

Investigating the role of fluid shear stress in bone metastasis: the proliferation of co-cultured hMSCs/MDAPCa2b cells under dynamic culturing.

Lahcen Akerkouch

North Dakota State University

Haneesh Jasuja

North Dakota State University

Kalpana Katti

North Dakota State University

Dinesh Katti

North Dakota State University

Trung Le (✉ trung.le@ndsu.edu)

North Dakota State University <https://orcid.org/0000-0002-4692-5469>

Research Article

Keywords: CFD, bone metastasis, fluid shear stress

Posted Date: July 13th, 2022

DOI: <https://doi.org/10.21203/rs.3.rs-1701124/v1>

License:  This work is licensed under a Creative Commons Attribution 4.0 International License.

[Read Full License](#)

1
2
3
4
5
6
7
8
9
10
11
12
13
14
15
16
17
18
19
20
21
22
23
24
25
26
27
28
29
30
31
32
33
34
35
36
37
38
39
40
41
42
43
44
45
46
47
48
49
50
51
52
53
54
55
56
57
58
59
60
61
62
63
64
65

1 Investigating the role of fluid shear stress in bone
2 metastasis: the proliferation of co-cultured
3 hMSCs/MDAPCa2b cells under dynamic culturing.

4 Lahcen Akerkouch¹, Haneesh Jasuja¹, Kalpana Katti¹, Dinesh Katti¹, and Trung Le¹

5 **Affiliations:** ¹Department of Civil, Construction and Environmental Engineering, North
6 Dakota State University, Fargo, ND, USA

7 **Correspondence:** Trung Le, Department of Civil, Construction and Environmental Engi-
8 neering, North Dakota State University, Fargo, ND, USA. e-mail: trung.le@ndsu.edu

1
2
3
4
5
6
7
8
9
10
11
12
13
14
15
16
17
18
19
20
21
22
23
24
25
26
27
28
29
30
31
32
33
34
35
36
37
38
39
40
41
42
43
44
45
46
47
48
49
50
51
52
53
54
55
56
57
58
59
60
61
62
63
64
65

Abstract

We investigated the potential correlation between the fluid shear stress and the proliferation of bone prostate cancer cells on the surface of nanoclay-based scaffolds in a perfusion bioreactor. Human mesenchymal stem cells (hMSCs) were seeded on the scaffolds to initiate bone growth. After 23 days, prostate cancer cells (MDAPCa2b) were cultured on top of the osteogenically differentiated hMSCs. The scaffolds were separated into two groups subjected to two distinct conditions: (i) static (no flow); and (ii) dynamic (with flow) conditions to recapitulate bone metastasis of prostate cancer. Based on measured data, Computational Fluid Dynamics (CFD) models were constructed to determine the velocity and shear stress distributions on the scaffold surface. Our experimental results show distinct differences in the growth pattern of hMSCs and MDAPCa2b cells between the static and dynamic conditions. Our computational results further suggest that the dynamic flow leads to drastic change in cell morphology and tumorous distribution. Our work points to a strong correlation between tumor growth and local interstitial flows in bones.

keywords: CFD; bone metastasis; fluid shear stress.

1 Introduction

Bone metastasis typically occurs at the advanced stages of cancer, mainly across the axial skeleton, such as the spine and pelvic bones,¹ where it leads to severe complications in patients, such as skeletal defects, resulting in high patient mortality. While it is unclear on the precise mechanisms cancer metastasis to bone, it is hypothesized that bone facilitates suitable micro-environment for cancer cells to grow.²

One important factor of the bone micro-environment is the impact of fluid flow. Bancroft et al. demonstrated an enhanced extracellular matrix generation by osteoblast cells when the flow rate increased from 0.3 to 3 mL/min in fibre mesh titanium scaffolds.³ On the other hand, substantial cell death was observed of MC3T3-E1 osteoblast-like cells at a flow rate of 1.0 mL/min in decellularized trabecular bone scaffolds.⁴ Furthermore, Yourek et al. investigated whether fluid flow-induced shear stress affects the differentiation of bone marrow-derived human mesenchymal stem cells (hMSCs) into osteogenic cells.⁵ Their results revealed an increased osteogenic differentiation of hMSCs subjected to shear stress at days 4 and 8 compared to those cultured in static conditions. Therefore, the impact of flow on hMSCs has been confirmed. However, it is unclear on the appropriate range fluid flow promotes the growth of hMSCs.

In addition to its impact on hMSCs, the role of fluid shear stress (FSS) was also emerged as a critical factor for tumor metastasis.⁶ Recent studies have provided evidence on the link between continuous fluid flow and cancer progression.⁷ In particular, the effect of FSS has been shown to impact cancer cells in many *in vitro* studies. For instance, the influence of FSS was observed in regulating endothelial barrier function and expression of angiogenic factors.⁸ However, there is a gap in knowledge on how fluid forces affect the growth of cancer cells as they arrest at the extravasation site. As the first step to address this gap in bone, our previous work (Figure 1a) consisted in developing a perfusion bioreactor to facilitate the co-culture of hMSCs and prostate cancer cells on nanoclay-based scaffolds under flow (dynamic) condition.⁹ The polymer nanoclay-based scaffolds are highly porous structures (86.1%), with pore size ranging from 10 to 300 μm while maintaining a high compressive

1
2
3
4
53 modulus of 2.495 *MPa*. It was observed that continuous fluid flow altered the orientation,
6
7
8
9
10
11
56 and morphology of prostate cancer cells and caused a change in their gene and protein
12
13
14
15
16
17
18
19
20
21
22
23
24
25
26
27
28
29
30
31
32
33
34
35
36
37
38
39
40
41
42
43
44
45
46
47
48
49
50
51
52
53
54
55
56
57
58
59
60
61
62
63
64
65
66
67
68
69
70
71
72
73
74
75
76
77
78
79
80
81
82
83
84
85
86
87
88
89
90
91
92
93
94
95
96
97
98
99
100
101
102
103
104
105
106
107
108
109
110
111
112
113
114
115
116
117
118
119
120
121
122
123
124
125
126
127
128
129
130
131
132
133
134
135
136
137
138
139
140
141
142
143
144
145
146
147
148
149
150
151
152
153
154
155
156
157
158
159
160
161
162
163
164
165

2 Methodology

2.1 Experimental protocols and configurations

2.1.1 Bioreactor design

The bioreactor chambers and their components were designed using *SolidWorks* software and fabricated using Formlabs Form-2 3D Printer as described in detail in our previous work.⁹ Briefly, the chambers were connected to the flow regulated pump and media bottles by silicone tubing (Peroxide-Cured Silicone, ID 1.42 *mm*, Ismatec). The flow rate was maintained at $Q = 0.2 \text{ mL}/\text{min}$ for all experiments. The chambers and media bottles were placed inside the incubator to maintain optimum conditions for cell survival at 37 °C, 5% CO_2 and high moisture (Figure 1a).

2.1.2 Preparation of the PCL/*in situ* HAP clay scaffolds

We have developed a protocol to prepare the scaffolds, and thus only short description of the procedure is described here.⁹ Briefly, sodium montmorillonite (Na-MMT) clay was modified with 5-aminovaleic acid amino acids modifiers to increase the d-spacing between clay sheets. Next, hydroxyapatite (HAP) was intercalated into the galleries of modified clay to form *in situ* HAP Clay. The scaffolds were prepared using freeze-drying method by mixing polycaprolactone (PCL) polymer and 10 *wt%* *in situ* HAP Clay.

2.1.3 Micro-CT Sample preparation and imaging

Scaffold samples were scanned using a micro-CT scanner (GE Phoenix vltomel xs X-ray computed tomography system) with 80 *kV* X-ray energy source and 350 μA current intensity with a molybdenum target. Scans were performed at multiple detector exposure times, 200 *ms*, 500 *ms*, 1000 *ms*, and 2000 *ms* in which the final image was reconstructed using a 500 *ms* detector timing. Sample magnification was carried out with a voxel size of 15.51 μm . The diameter and thickness of the scaffold were estimated as approximately 12 *mm* and 3 *mm*, respectively. The micro-CT image of the scaffold in Figure 1b shows that the scaffold possesses interconnected pores, which are necessary for fluid flow to travel through the scaffolds.

2.1.4 Cell culturing and seeding

Human mesenchymal stem cells (hMSCs Lonza, PT-2501) were cultured in MSCGM Bullet kit medium (Lonza, PT-3001). An amount of 5×10^5 hMSCs cells were seeded on each scaffold in a 24-well plate and incubated at 37 °C and 5% *CO*₂ inside the incubator for 24 hours, considered as Day-0 as shown in Figure 2.

After 24 hours, the hMSCs seeded scaffolds are separated into two groups subjected to different hydrodynamic conditions. The first half of the scaffolds remained in the incubator (static condition). The remaining half of the hMSCs seeded scaffolds were transferred into the bioreactor followed by culturing for 23 days for their osteogenic differentiation (dy-

1
2
3
4
5
6
7
8
9
10
11
12
13
14
15
16
17
18
19
20
21
22
23
24
25
26
27
28
29
30
31
32
33
34
35
36
37
38
39
40
41
42
43
44
45
46
47
48
49
50
51
52
53
54
55
56
57
58
59
60
61
62
63
64
65

102 namic condition). In separate essays, human prostate cancer (PCa) cells line MDAPCa2b
103 (ATCC[®] CRL-2422[™]) were cultured in media comprised of 80% BRFF-HPC1 (AthenaES,
104 0403), 20% fetal bovine serum (FBS) (ATCC, 30-2020), and 1% Penicillin–Streptomycin
105 (Gibco).

106 After 23 days, 1×10^5 cells of prostate cancer were seeded on bone containing scaffolds
107 under static and dynamic conditions. Note that the scaffolds were removed from the biore-
108 actor for cell seeding purpose. They were transferred back into their respective locations
109 after 4 hours of incubation.

110 Prostate cancer cells seeded on bone scaffolds were cultured for 20 days under both
111 conditions. Media was changed every 2 days for static cultures and every 3 days for dynamic
112 cultures. hMSCs and PCa media were utilized in 1:1 ratio after PCa cells seeding step. Note
113 that both hMSC and PCa cells were seeded on the back surface of the scaffold. The rationale
114 for this protocol will be further discussed in the experimental results section.

115 **2.1.5 Cell viability**

116 The hMSCs viability was determined under static and dynamic conditions using WST-1
117 reagent (Roche) as per the manufacturer’s protocol. In brief, cell-seeded scaffolds were
118 removed from the culture medium on Day-0, Day-5, and Day-10 then washed twice with
119 PBS. Scaffold samples seeded with hMSCs in a 24-well plate under static conditions and
120 incubated at $37^\circ C$, 5% CO_2 for 24 hours with Day-0 considered as the Control. Next, the
121 scaffolds were placed in a new 24-well plate with a solution containing DMEM-12 and WST-1
122 reagent (1:1) and incubated for 4 hours in an incubator. After incubation, the intensity of
123 yellow color was measured at 450 *nm* using a microplate spectrophotometer (Bio-Rad). The
124 change in color from a slight red to yellow occurs due to the cleaving of tetrazolium salts of
125 WST-1 reagent to formazan by metabolically active cells.

2.1.6 Live-dead assay and DAPI staining

The viability of hMSCs was examined by live/dead staining (Biotium, 30002-T). The scaffolds containing hMSCs at different time points (Day-0, Day-10, and Day-23 in Figure 2) under both conditions were rinsed twice with warm PBS. Further, the scaffolds were incubated in a solution containing $2 \mu\text{M}$ calcein AM and $4 \mu\text{M}$ Ethidium Homodimer III (EthD-III) in PBS for 30 *min* at room temperature for staining live cells and dead cells, respectively as per manufacturer's protocol. The scaffolds were imaged under Zeiss Axio Observer Z1 LSM 700 confocal microscope using Ex/Em wavelengths described in manufacturer's protocol.

To assess the distribution of hMSCs on the scaffold surface, all four scaffold samples were retrieved from the bioreactor chamber and cells were fixed using 4% paraformaldehyde solution. Next, the cells were counterstained with 4,6-diamidino-2-phenylindole (DAPI), and images were taken under Zeiss Axio Observer Z1 LSM 700 confocal microscope.

2.1.7 Histologic examination

The samples were fixed with 4% formaldehyde, dehydrated in graded series of ethanol, and embedded in paraffin wax. Consecutive sections were cut from the paraffin blocks into $5 \mu\text{m}$ slides, sections were deparaffinized and stained with Hematoxylin and Eosin to assess cell distribution on the scaffold surface.

2.1.8 Scanning Electron Microscopy (SEM)

The samples containing hMSCs and sequentially cultured PCa cells were retrieved from both culturing conditions on Day-23, Day-(23 + 10), and Day-(23 + 20), respectively and washed twice with PBS. Further, the cells on the scaffolds were fixed with 2.5% glutaraldehyde overnight at 4°C . Next, the cells were dehydrated with ethanol series (30%, 50%, 70%, 90%, and 100%), and the scaffolds were dried using hexamethyldisilazane. The dried scaffolds were sputter-coated with gold and mounted on SEM stubs for scanning under the scanning electron microscope (JEOL JSM-6490LV).

2.2 Numerical simulation

2.2.1 Bioreactor geometrical model

From the bioreactor design (Figure 1), the computational models are reconstructed as seen in Figure 3. The bioreactor’s inlet and outlet are circular tubes with diameters of 1 mm. As seen in Figure 3a, the diameter and length of the bioreactor chamber are 17 mm and 45 mm, respectively. The *SolidWorks* model of the bioreactor was converted to the STereoLithography (STL) format, and re-meshed as an unstructured mesh. At the inlet, a uniform flow velocity of 4.24 mm/s is applied for all cases.

2.2.2 Scaffold geometry

There is a large disparity of fluid flow scale within the bioreactor across several orders of magnitudes. The flow structures varies from millimeter scale (bioreactor inlet) to micrometers (scaffold pores). It is challenging to resolve all the flow features in the bioreactor with the existing computational resources. Therefore, a multi-scale approach is carried out to resolve the flow structures systematically.

Here, we consider two types of scaffolds to provide the estimations of millimeter as well as the micrometer scale flow patterns. First, an idealized model of the scaffolds is considered as an impervious cylindrical body. As shown in Figure 3b, the diameter and thickness of this model are 12 mm and 3 mm, respectively. This idealized model is used to provide a general (large-scale) pattern of the flow inside the bioreactor and the surrounding areas of scaffolds. Second, the realistic scaffold model is re-constructed from the micro-CT data (Figure 1b). Note that this realistic model only considers pores with a diameter larger than 70 μm due to the resolution limit of the micro-CT scan. The cross-section view in Figure 1b highlights the highly interconnected pores, which are necessary for the interior fluid flows. The open-source software *Slicer3D* is used to generate the full-scale 3D surface mesh of the scaffold. The STL model of the scaffold was smoothed and re-surfaced using the open-source software *Meshmixer* (Figure 1c). The details of the two types of scaffolds are explained in

1
2
3
4
5 177 Table 1.
6
7

8 178 **2.2.3 Numerical methods**

9
10 179 The DMEM fluid was considered to be an incompressible Newtonian fluid with constant
11
12 180 density ($\rho = 1000 \text{ kg/m}^3$) and kinematic viscosity ($\nu = 0.78 \times 10^{-6} \text{ m}^2/\text{s}$).⁹ The numerical
13
14 181 method employed in this work has been extensively described and thoroughly validated
15
16 182 against *in vitro* and *in vivo* data for millimeter to micrometer scales. Therefore, only a brief
17
18 183 description of the numerical method is presented in this section. For more details about the
19
20 184 method, the reader is referred to our previous publications.^{10,11} The governing equations for
21
22 185 the fluid are modeled as three-dimensional Navier-Stokes equations. The governing equations
23
24 186 are solved using the sharp-interface curvilinear-immersed boundary (CURVIB) method in
25
26 187 a background curvilinear domain that contains the complex geometries of the bioreactor
27
28 188 and scaffold models. The discrete equations are integrated in time using a fractional step
29
30 189 method. A Newton-Krylov solver is used to solve the momentum equations in the momentum
31
32 190 step, and a Generalized Minimal Residual (GMRES) solver with multigrid preconditioner is
33
34 191 employed for the Poisson equation. The details of the computational code can be found at
35
36 192 <https://www.osti.gov/biblio/1312901-virtual-flow-simulator>.
37
38
39
40

41 193 **2.2.4 Computational setups**

42
43 194 A multi-scale approach to investigate the flow around the scaffold was carried out. First,
44
45 195 the flow around the scaffolds was examined in large-scale patterns (millimetre scale) to
46
47 196 understand the impacts of the scaffolds arrangement on the FSS distribution. Second, the
48
49 197 overall distribution of FSS on each scaffold was examined to investigate the blocking effect of
50
51 198 consecutive scaffolds. Finally, the internal flow inside each scaffold is studied via a series of
52
53 199 high-fidelity simulations to resolve individual pores in four computational setups as discussed
54
55 200 below.
56

57
58 201 First, the large-scale model is simulated using the entire bioreactor chamber (Case A)
59
60 202 without any scaffolds. The 3D surface mesh of the empty bioreactor is illustrated in Figure
61
62
63
64
65

1
2
3
4
5
6
7
8
9
10
11
12
13
14
15
16
17
18
19
20
21
22
23
24
25
26
27
28
29
30
31
32
33
34
35
36
37
38
39
40
41
42
43
44
45
46
47
48
49
50
51
52
53
54
55
56
57
58
59
60
61
62
63
64
65

203 3a. The details of the bioreactor mesh are shown in Table 1. The simulation setup is used to
204 investigate the large-scale flow patterns inside the bioreactor in the absence of the scaffolds.

205 Second, the role of the scaffolds in changing the large-scale flow pattern within the biore-
206 actor is examined. In addition to the computational setup of Case A, four idealized scaffolds
207 were placed within the bioreactor as shown in Figure 3b, their details are shown in Table 1.
208 The locations of the idealized scaffolds are in the exact arrangement as in the experimental
209 settings. The first scaffold locates at a distance of 6 mm from the bioreactor inlet, and each
210 two consecutive scaffolds are separated with 6 mm from each other as shown in Figure 3b.
211 Due to the idealized geometry, no pores are considered in this computational configuration.
212 Two specific surfaces of the idealized scaffolds are of interest: (i) the front, and (ii) the
213 back surfaces. The front and back surfaces denotes the upstream and downstream sides of
214 the scaffold as shown in Figure 1c. The role of these surfaces is discussed further in the
215 simulation results section.

216 Third, the flow pattern inside the scaffold’s pores is examined in Case C. The compu-
217 tational domain is defined as a rectangular box (Figure 3c) with the similar dimensions to
218 the bioreactor chamber. To capture accurately the intricate porous geometry, the micro-CT
219 scaffold model is represented with highly dense unstructured mesh with more than half mil-
220 lion surface elements (triangles) as depicted in Figure 1c and Table 1. Due to this complexity
221 of the scaffold’s porosity architecture, a high number of grid points (more than 64 million)
222 in the computational domain is needed to resolve the flow and FSS at the level of the pores
223 as shown in Table 2.

224 Fourth, Case D is used to investigate the impacts of the blocking effect by the scaffolds
225 on the local FSS at the entire surface volume of the scaffold. Two full-scale scaffolds were
226 placed inside the computational domain. Following the same experimental arrangement, the
227 two scaffolds are 6 mm apart for each other. The computational domain is a box of size
228 17 mm × 17 mm × 25.5 mm as seen in Figure 3d and Table 2.

229 In all four cases, an inlet uniform velocity profile was applied. The Neumann bound-
230 ary condition was specified for all velocity components at the outlet. No-slip and no-flux

1
2
3
4 231 conditions are prescribed at all boundary walls, which are considered rigid. In subsequent
5
6 232 sections, the steady state solutions of the simulations are reported for the flow and FSS
7
8
9 233 patterns.

10 11 12 13 234 **3 Results**

14 15 16 235 **3.1 The dependence of hMSCs growth on hydrodynamic condi-** 17 18 19 236 **tions**

20
21
22 237 The measured absorbance at 450 *nm* wavelength in Figure 5 showed that the viability of
23
24 238 hMSCs increased on Day-10 when the homeostatic condition was attained (no flows). At
25
26 239 first, the absorbance showed a slight increase in cell proliferation from Day-0 (control) to
27
28 240 Day-5. However, a significant increase ($*p < 0.05$) of cell viability was observed from Day-5
29
30 241 to Day-10 as shown in Figure 4b. Therefore, the static condition promotes the culturing of
31
32 242 hMSCs.

33
34 243 Under dynamic condition, the hMSCs proliferation was observed to increase significantly
35
36 244 from Day-0 to Day-10 when they were under continuous flow rate of $Q = 0.2 \text{ mL/min}$
37
38 245 (dynamic condition). Due to the difference in hydrodynamic conditions, the scaffolds have
39
40 246 two distinct surfaces: (*i*) front; and (*ii*) back surfaces under dynamic condition. The front
41
42 247 surface faces the flow direction while the back surface locates at the downstream side of
43
44 248 the scaffold. The difference in hydrodynamic conditions produced distinct trends in cell
45
46 249 proliferation. As evident in Figure 4a, seeding the hMSCs on the front surface of scaffolds led
47
48 250 to a major cell death at Day-10. In particular, the viability of hMSCs decreased significantly
49
50 251 ($**p < 0.01$) from Day-0 to Day-10. On the contrary, in Figure 4b the hMSCs showed a clear
51
52 252 preference in proliferating on the back surface. Because the hMSCs did not proliferate on
53
54 253 the front surface, they were seeded only on the back surface of the scaffold in subsequent
55
56 254 experiments within the perfusion bioreactor (Figures 5a-b).

57
58
59 255 Under dynamic condition, a significant increase in cell proliferation and morphological
60
61
62
63
64
65

1
2
3
4
5
6
7
8
9
10
11
12
13
14
15
16
17
18
19
20
21
22
23
24
25
26
27
28
29
30
31
32
33
34
35
36
37
38
39
40
41
42
43
44
45
46
47
48
49
50
51
52
53
54
55
56
57
58
59
60
61
62
63
64
65

change were observed. There existed non-uniform presence of DAPI stained hMSCs nuclei in all four scaffolds at Day-23 as seen in Figure 5b. Furthermore, the hMSCs were observed to be stretched in a well-defined direction under the impact of fluid forces as seen in Figures 5c-d as opposed to the random distribution of hMSCs under static condition on the Day-23. Based on the qualitative assessment of the cell viability by live-dead staining assay shown in Figure 5c, almost all the hMSCs were observed alive along the period of 23 days. In addition, the hMSCs gained a directional orientation even early on Day-10 under dynamic condition as shown in Figure 5c. On Day-23, SEM analysis of hMSCs under dynamic and static culturing are shown in Figures 5e-f. Under dynamic condition (Figure 5f), the cells aligned to well-defined orientation, whereas under static condition they exhibited cell aggregation (Figure 5e). In brief, the presence of a dynamic condition altered the large scale distribution of cells as well as the local cellular morphology.

3.2 Morphological changes of co-cultured hMSCs/MDAPCa2b cells under continuous flow

After culturing (static and dynamic) the seeded hMSCs for a period of 23 days for osteogenic differentiation and mineralized bone formation, prostate cancer cells (MDAPCa2b) were seeded on the top of the osteogenically differentiated hMSCs for a period of 20 days (Day-(23 + 20)). Hematoxylin and eosin staining were employed to visualize the distribution of the co-cultured hMSCs + MDAPCa2b on the surface of the scaffolds on Day-(23 + 20) under static and dynamic conditions as seen in Figure 6. The morphological changes in prostate cancer cells and their distribution within scaffold under static and dynamics culturing were evaluated utilizing the SEM technique as well. To reflect the morphological changes under fluid flow, the results were both reported of the co-cultured cells on Day-(23 + 10) and Day-(23 + 20).

The results revealed a clear impact of the flow on the co-cultured hMSCs/MDAPCa2b growth. Under static condition the staining of hMSCs + MDAPCa2b showed that the cells nuclei were randomly distributed on the scaffold surface as seen in Figures 6a-b. However, a

1
2
3
4
5 283 striking feature of cellular distribution was found on the edges of the pores under dynamic
6
7 284 condition as shown in Figures 6c-d. Cell proliferation was found mostly to occur in the
8
9 285 vicinity of scaffold's pores.

10
11 286 The local impact of the flow on the MDAPCa2b's morphology is further shown in Figure
12
13 287 7. Under static condition, the MDAPCa2b cells were observed to form tumors with round
14
15 288 (spherical) morphology on Day-(23 + 10). The cells maintained such morphology till Day-
16
17 289 (23 + 20) with an increased in tumor size as seen in Figures 7a and 7c. On the contrary,
18
19 290 MDAPCa2b prostate cancer cells appeared to undergo a significant morphology change on
20
21 291 Day-(23 + 10) under dynamic culture. Their morphology was observed to consistently change
22
23 292 over time, and appeared to form compact structures with no distinct boundaries on Day-(23
24
25 293 + 20) as shown in Figures 7b and 7d. Interestingly, the MDAPCa2b cells were shown to
26
27 294 grow surrounding the pores of scaffolds under dynamic conditions in agreement with their
28
29 295 large-scale distribution shown in Figure 6c-d. Hence, our results showed a clear impact of
30
31 296 continuous flow on the growth of co-cultured hMSCs/MDAPCa2b cells, especially around
32
33 297 the pores as shown in Figures 7e-f.

37 298 **3.3 Large-scale flow patterns**

38
39
40 299 In case A, the flow velocity distribution within the empty perfusion bioreactor was shown
41
42 300 in Figure 8a. Due to the low applied Reynolds number, the flow within the bioreactor
43
44 301 resembled closely to a Poiseuille flow profile except areas at the inlet and outlet. In particular,
45
46 302 at the center of the bioreactor, the velocity magnitude was observed significantly lower
47
48 303 ($\sim 50 \mu m/s$). The bioreactor design provided a consistent flow condition along the chamber
49
50 304 axis.

51
52 305 In case B, four idealized scaffolds were placed within the bioreactor to investigate their
53
54 306 influence on the local flow pattern and the direction of the FSS on the surface of the scaffolds,
55
56 307 as depicted in Figures 8b-c. The presence of the idealized scaffolds altered significantly the
57
58 308 overall distribution of the laminar fluid flow within the bioreactor as compared to Case
59
60 309 A. Moreover, the flow velocity between the scaffold edge and the bioreactor chamber wall

1
2
3
4 310 increased significantly up to $100 \mu m/s$. In addition, a blocking effect was observed at the
5
6 311 gaps between the scaffolds where the velocity magnitude was very low (up to $20 \mu m/s$).
7
8 312 This blocking effect was even more evident as it influenced the orientation of the FSS on the
9
10 313 surface of the idealized scaffolds. On the first scaffold, the FSS diverged immediately toward
11
12 314 the edge after the flow impacted the scaffold front surface. The FSS pattern converged toward
13
14 315 the center of the back surface following the flow direction. Under the presence of the second
15
16 316 scaffold, a flow circulation was created inside the space between the first and the second
17
18 317 scaffolds. Therefore, the FSS on the back of the first scaffold converged to a circulation zone
19
20 318 as evident by a separation line near the back surface center. In this circulation zone, the
21
22 319 FSS magnitude was observed to be less than $20 \mu Pa$. This circulation pattern appeared on
23
24 320 the back surface of the second and third scaffolds as well. On the back surface of the fourth
25
26 321 scaffold, the FSS pattern converged back to center of scaffold's back surface since there was
27
28 322 no blocking effect.
29
30
31
32

323 **3.4 Flow in the vicinity of pores**

33
34
35 324 In case C, the velocity and shear stress distributions were examined at the level of the
36
37 325 pore resolution (Figure 3c). Overall, the FSS distribution on the scaffold front and back
38
39 326 surfaces (Figures 9a-b) revealed that the FSS exhibited a heterogeneous distribution on the
40
41 327 surfaces depending on the presence of the pore geometries. The FSS contour revealed that
42
43 328 the majority of FSS on both surfaces of the scaffold fell into the interval $[0 - 15] \mu Pa$. The
44
45 329 maximum FSS magnitude (greater than $50 \mu Pa$) occurred at the boundaries of the scaffold
46
47 330 due to the narrow space between the edge of the scaffold and the domain wall. In addition,
48
49 331 there was a large hole in the center of the scaffold leading to a flow convergence region near
50
51 332 the hole. To illustrate the orientation of the FSS, the FSS vectors on the front and back
52
53 333 surfaces of the scaffold were plotted in Figure 9c-d. The results showed that the direction of
54
55 334 FSS vectors followed closely the geometry of the scaffold pores. On the front surface, FSS
56
57 335 vectors diverged toward the edges of the scaffold, except the area close to the central hole.
58
59 336 On the back surface, the FSS pattern was more complex. The overall pattern consisted of
60
61
62
63
64
65

1
2
3
4
5
6
7
8
9
10
11
12
13
14
15
16
17
18
19
20
21
22
23
24
25
26
27
28
29
30
31
32
33
34
35
36
37
38
39
40
41
42
43
44
45
46
47
48
49
50
51
52
53
54
55
56
57
58
59
60
61
62
63
64
65

337 convergence zones surrounding the pores as shown in Figure 9d. In brief, there was a clear
338 distinction of the FSS characteristics between the front and back surfaces of the scaffold.

339 To further analyze the difference between the hydrodynamic conditions on the scaffold's
340 front and back surfaces, the histograms of the flow velocity and FSS were plotted for layers
341 close to the surfaces (0.8 mm thickness) in Figures 9e-f. Our results demonstrated that
342 there was a significant difference on the approaching flow velocity distribution between the
343 front and the back surfaces as shown in Figure 9e. Our results revealed that the fluid flow
344 velocities on the front surface of the scaffold were observed to distribute evenly across all
345 magnitudes up to 10 $\mu m/s$. On the contrary, the fluid flow velocity on the back surface
346 was observed to fall almost exclusively (85%) in the interval of $[0 - 0.05] \mu m/s$. Despite the
347 difference in the flow velocities between the front and back surfaces, the FSS histograms in
348 Figure 9f showed a consistent distribution pattern.

349 In order to verify the hydrodynamic conditions inside the scaffold, three horizontal planes,
350 which are in the position of 25%, 50%, and 75% thickness, were used as shown in Figure
351 10. It is evident in Figure 10a that flow the velocity was largely dependent on the pore
352 architecture. The presence of the central hole induced a high velocity region (greater than
353 2 $\mu m/s$) in the scaffold's center. In addition, the complex geometry of the pores guided
354 local high velocity regions inside the scaffold with the existence of high velocity patches. To
355 quantify the similarity in flow and FSS distribution on these planes, the frequency histograms
356 in Figures 10c-d were used to compare the hydrodynamic conditions among these planes.
357 Despite the geometrical irregularity, the horizontal plane cuts in Figure 10b revealed a similar
358 frequency distribution of FSS among the three horizontal planes. The FSS value was mostly
359 less than 10 μPa in all planes. The majority of the fluid flow velocities were within the
360 interval of 0.1 to 5 $\mu m/s$ inside the scaffold as shown in Figure 10c, in which the range of
361 the FSS magnitude was mostly between 1 and 10 μPa . Our results thus depicted that the
362 overall distribution of flow velocity remained rather consistent across all three planes.

3.5 The hydrodynamic impact of scaffold arrangement

The scaffold arrangement has a minimal impact on the approaching velocity and shear stress distribution of the scaffold. As shown in Figure 11a, the velocity field between two consecutive scaffolds was observed complex. The second scaffold creates a blocking effect by inducing a reduction of flow velocity (less than $2 \mu\text{m}/\text{s}$) in the gap between these scaffolds. This reduction creates a flow circulation zone, which covered almost entirely the gap. To examine the effect of this gap, the flow velocity and FSS at different cross-sections (25%, 50%, 75% in Figure 11b) of the first scaffold are computed. Their histograms showed consistent patterns of hydrodynamics at all cross-sections as shown in Figures 11c-d. The majority of the flow velocities were within the range of $[0.1 - 5] \mu\text{m}/\text{s}$, while most of the FSSs occurred from $1 \mu\text{Pa}$ and above as seen in Figures 11c-d. Comparing with the histograms in Figures 10 and 11, it is evident that the impact of the second scaffold is insignificant.

4 DISCUSSION

Dynamic culturing has been shown to accelerate the hMSCs proliferation and differentiation, in which the FSS induced by interstitial flow is considered a key parameter in activating, and maintaining the proliferation and differentiation of hMSCs for bone growth.⁹ In the current study, we developed a 3D *in vitro* perfusion bioreactor model using high interconnective porous scaffolds to replicate the *in vivo* conditions of the interstitial fluid transport in bone. Overall, our numerical and experimental results indicate that our current bioreactor design achieved the *in vivo* conditions. For instance, the flow velocities between the scaffolds and on the scaffold surface (Case B) were observed between 0 and $20 \mu\text{m}/\text{s}$, which are within the physiological range of the interstitial flow.¹² The fluid-induced shear stress on the surface of the scaffolds (Case B) was observed to reach a magnitude up to $60 \mu\text{Pa}$. Our previous work also demonstrated that the proliferation and osteogenic differentiation of hMSCs were enhanced under FSS of approximately $10 \mu\text{Pa}$.⁹ Our results in Figure 8 showed that FSS in our bioreactor attained the magnitude up to $100 \mu\text{Pa}$. Note that *in vitro* experiments

1
2
3
4
5
6
7
8
9
10
11
12
13
14
15
16
17
18
19
20
21
22
23
24
25
26
27
28
29
30
31
32
33
34
35
36
37
38
39
40
41
42
43
44
45
46
47
48
49
50
51
52
53
54
55
56
57
58
59
60
61
62
63
64
65

389 have shown that significant osteogenic differentiation of hMSCs occurs under FSS range of
390 $[10 - 1000] \mu Pa$.¹³ Thus, our bioreactor design is able to provide physiological FSS values
391 to promote bone formation.

392 There is a variation of hydrodynamic conditions and the associated cellular growth among
393 scaffolds as shown in Figures 5 and 8. First, the cell viability showed the signatures of
394 hMSCs proliferation across all back surfaces of the four scaffolds (Figure 5b). However,
395 there exist a considerable difference on the cell distribution pattern (blue pixels). To explain
396 this phenomenon, we re-examined the shear stress patterns on each scaffold separately using
397 the large-scale simulation (Case B) in Figure 8. While FSS diverges toward the edges on
398 the front surface, it converges toward the center on the back surface in the first scaffold.
399 This convergence coincides with the proliferation of cells on the back surface, which is not
400 observed on the front surface (Figure 2). Moreover, the FSS magnitude is much lower on the
401 back surface (less than $10 \mu Pa$) in comparison to the one on the front surface ($\sim 60 \mu Pa$)
402 as seen in Figure 8c. This observation suggests that the hMSCs can only proliferate under
403 low shear stress. Indeed, the consecutive placement of the scaffolds created low flow and low
404 shear stress regions between the scaffolds as shown in Figures 8b-c. The FSS magnitude on
405 the second, third, and fourth scaffold did not go beyond $20 \mu Pa$. The cells were able to grow
406 on the back surfaces of these scaffolds as shown in Figure 5. In brief, our work suggests that
407 the magnitude of FSS should be within $[10 - 20] \mu Pa$ to promote bone growth.

408 The distribution of FSS has been hypothesized to be dependent on scaffold's pore size
409 and architecture.¹⁴ Therefore, it is critical to resolve the scaffold geometries accurately.
410 However, resolving flow condition in the pores of the full-scale 3D scaffold is a challenging
411 task. The complexity of the porous structures requires a sufficiently fine mesh to accurately
412 capture the pores as shown in Table 1. Past works simplified the computational domain
413 and focused only on sub-domains, which are local regions of the scaffold.¹⁵ In the present
414 study, numerical simulations were performed using the entire scaffold geometry (micro-CT
415 scan) to provide a realistic distribution of FSS within the pores. Our computational data
416 showed strong evidence of correlation between the FSS direction, scaffold porosity and the

1
2
3
4
5
6
7
8
9
10
11
12
13
14
15
16
17
18
19
20
21
22
23
24
25
26
27
28
29
30
31
32
33
34
35
36
37
38
39
40
41
42
43
44
45
46
47
48
49
50
51
52
53
54
55
56
57
58
59
60
61
62
63
64
65

417 cells proliferation. Our high-resolution simulation (Case C) in Figure 9 shows that FSS
418 distribution is heterogeneous on the scaffold surfaces. In particular, the shear stress pattern
419 on the back surface of the scaffold (Figure 9b) indicates an intricate flow surrounding the
420 pore holes. The FSS was observed to converge around the pores creating a shear dominant
421 direction (Figures 9c-d). Our histological observations in Figures 6c-d indicated a localized
422 growth of cells near the edges of the pores under dynamic condition, where a such localized
423 growth was not observed in the static condition both in the large-scale (Figure 6a) nor
424 locally near the pores (Figure 6b). Under the static condition, the patterns of the hMSCs
425 and prostate cancer cells were randomly distributed. Under dynamic condition, the cells
426 grew locally in the vicinity of the pores where the shear stress is high as shown in Figure
427 7. The distribution and morphology of prostate cancer cells on Day-(23 + 10) and Day-(23
428 + 20) under dynamic condition in Figure 7 also showed a similar trend. Moreover, the
429 morphological orientation of individual cells in Figures 5b, 6, and 7 agreed well with the
430 direction of the applied FSS (Figure 9c-d). Based on our experimental and computational
431 studies, we found that FSS significantly altered the distribution, morphology and growth of
432 the co-cultured hMSCs and prostate cancer cell. Therefore, our work suggests that FSS is
433 responsible on regulating the distribution of cells on the pore edges.

434 Another advantage of this approach is the ability to resolve the flow circulation zone
435 between two consecutive scaffolds as illustrated in Figure 11a. Our results showed that
436 the velocity and shear stress distributions on the first scaffold were minimally affected by
437 the presence of the second scaffold (Figures 10c-d and 11c-d). This analysis indicates that
438 the approaching velocity on the scaffold surfaces is mostly in the range of $[0.1 - 5] \mu m/s$,
439 and the fluid-induced shear stress is approximately around $[1 - 10] \mu Pa$. Therefore, future
440 experimental works can utilize these ranges in designing three-dimensional tumor models.

5 CONCLUSION

A series of experimental and computational works were carried out to investigate the impacts of fluid shear stress (FSS) on the growth of co-cultured hMSCs and prostate cancer cells on the surface of bone scaffolds within a perfusion bioreactor. Our conclusions are:

- Within each scaffold, the flow velocity distribution is highly heterogeneous due to the complex distribution of pores. There exist a correlation between the pore size and the local flow velocity.
- The cellular viability depends on the local hydrodynamic condition. The appropriate flow velocity and shear stress are found to be $[0.1 - 5] \mu m/s$ and $[1 - 10] \mu Pa$, respectively.
- Under dynamic condition, the morphology of the hMSCs is stretched along a preferred direction. We hypothesize that the stretching direction coincides to the local direction of the FSS.
- The proliferation of MDAPCa2b cells is enhanced significantly at the boundaries of the pores, which coincides to the convergence of the local direction of FSS. We hypothesize that the local increase in FSS favors the growth of MDAPCa2b.

Conflict of Interest

The authors have no conflicts of interest to declare.

Acknowledgment

This work is supported by the NSF grant number 1946202 (ND-ACES) and a start-up package of Trung Le from North Dakota State University. The authors acknowledges the use of computational resources at the Center for Computationally Assisted Science and

1
2
3
4
5 463 Technology (CCAST)-NDSU, which is supported by the NSF MRI 2019077. The authors also
6
7 464 received an allocation (CTS200012) from the Extreme Science and Engineering Discovery
8
9 465 Environment (XSEDE). We acknowledge the financial support of NIH-2P20GM103442-19A1
10
11 466 to train undergraduate students in Biomedical Engineering.
12
13
14

15 467 **References**

- 16
17
18 468 1. Roodman G.D. Mechanisms of bone metastasis. *N Engl J Med*, 350(16):1655–1664,
19
20 469 2004.
- 21
22
23 470 2. Molla M.D.S., D.R. Katti, and K.S. Katti. In vitro design of mesenchymal to epithelial
24
25 471 transition of prostate cancer metastasis using 3d nanoclay bone-mimetic scaffolds. *J*
26
27 472 *Tissue Eng Regen Med*, 12(3):727–737, 2018.
- 28
29
30 473 3. Bancroft G.N., V.I. Sikavitsas, J.V.D. Dolder, T.L. Sheffield, C.G. Ambrose, J.A. Jansen,
31
32 474 and A.G. Mikos. Fluid flow increases mineralized matrix deposition in 3d perfusion
33
34 475 culture of marrow stromal osteoblasts in a dose-dependent manner. *PNAS*, 99(20):12600–
35
36 476 12605, 2002.
- 37
38
39 477 4. Cartmell S.H., B.D. Porter, A.J. Garcia, and R.E. Guldborg. Effects of medium perfu-
40
41 478 sion rate on cell-seeded three-dimensional bone constructs in vitro. *Tissue engineering*,
42
43 479 9:1197–1203, 2003.
- 44
45
46 480 5. Yourek G., S.M. McCormick, J.J. Mao, and G.C Reilly. Shear stress induces osteogenic
47
48 481 differentiation of human mesenchymal stem cells. *Regenerative Medicine*, 5(5):713, 2010.
- 49
50
51 482 6. Polacheck W.J., J.L. Charest, and R.D. Kamm. Interstitial flow influences direction of tu-
52
53 483 mor cell migration through competing mechanisms. *Proc Natl Acad Sci*, 108(27):11115–
54
55 484 20, 2011.
- 56
57
58 485 7. Shah A.D., M.J. Bouchard, and A.C. Shieh. Interstitial fluid flow increases hepatocel-
59
60
61
62
63
64
65

1
2
3
4
5
6
7
8
9
10
11
12
13
14
15
16
17
18
19
20
21
22
23
24
25
26
27
28
29
30
31
32
33
34
35
36
37
38
39
40
41
42
43
44
45
46
47
48
49
50
51
52
53
54
55
56
57
58
59
60
61
62
63
64
65

486 lular carcinoma cell invasion through cxcr4/cxcl12 and mek/erk signaling. *PLoS One*,
487 10(11):e0142337, 2015.

488 8. Buchanan C.F., S.S. Verbridge, P.P. Vlachos, and M.N. Rylander. Flow shear stress
489 regulates endothelial barrier function and expression of angiogenic factors in a 3d mi-
490 crofluidic tumor vascular model. *Cell Adh Migr*, 8(5):517–24, 2014.

491 9. Jasuja H., S. Kar, D.R. Katti, and K.S. Katti. Perfusion bioreactor enabled fluid-derived
492 shear stress conditions for novel bone metastatic prostate cancer testbed. *Biofabrication*,
493 13:035004, 2021.

494 10. Ge L. and F. Sotiropoulos. A numerical method for solving the 3d unsteady incompress-
495 ible navier–stokes equations in curvilinear domains with complex immersed boundaries.
496 *J. Comput. Phys*, 225:1782–1809, 2007.

497 11. Akerkouch L. and T.B. Le. A hybrid continuum-particle approach for fluid-structure
498 interaction simulation of red blood cells in fluid flows. *Fluids*, 6(4):139, 2021.

499 12. Hajal C., I. Lina, S.J. Carlos, G.S. Offeddu, and R.D. Kamm. The effects of luminal
500 and trans-endothelial fluid flows on the extravasation and tissue invasion of tumor cells
501 in a 3d in vitro microvascular platform. *Biomaterials.*, 265:120470, 2020.

502 13. Gao X., X. Zhang, H. Xu, B. Zhou, W. Wen, and J. Qin. Regulation of cell migration
503 and osteogenic differentiation in mesenchymal stem cells under extremely low fluidic
504 shear stress. *Biomicrofluidics.*, 8:052008, 2014.

505 14. Zermatten E., J.R. Vetsch, D. Ruffoni, S. Hofmann, R. Muller, and A. Steinfeld.
506 Micro-computed tomography based computational fluid dynamics for the determina-
507 tion of shear stresses in scaffolds within a perfusion bioreactor. *Ann Biomed Eng*,
508 42(5):1085–1094, 2014.

509 15. Zhao F., J. Melke, K. Ito, B.V. Rietbergen, and S. Hofmann. A multiscale computa-
510 tional fluid dynamics approach to simulate the micro-fluidic environment within a tissue

1
2
3
4
5
6
7
8
9
10
11
12
13
14
15
16
17
18
19
20
21
22
23
24
25
26
27
28
29
30
31
32
33
34
35
36
37
38
39
40
41
42
43
44
45
46
47
48
49
50
51
52
53
54
55
56
57
58
59
60
61
62
63
64
65

511
512

engineering scaffold with highly irregular pore geometry. *Biomech Model Mechanobiol*,
18(6):1965–1977, 2019.

1
2
3
4
5
6
7
8
9
10
11
12
13
14
15
16
17
18
19
20
21
22
23
24
25
26
27
28
29
30
31
32
33
34
35
36
37
38
39
40
41
42
43
44
45
46
47
48
49
50
51
52
53
54
55
56
57
58
59
60
61
62
63
64
65

513

[Table 1 about here.]

1
2
3
4
5
6
7
8
9
10
11
12
13
14
15
16
17
18
19
20
21
22
23
24
25
26
27
28
29
30
31
32
33
34
35
36
37
38
39
40
41
42
43
44
45
46
47
48
49
50
51
52
53
54
55
56
57
58
59
60
61
62
63
64
65

514

[Table 2 about here.]

1
2
3
4
5
6
7
8
9
10
11
12
13
14
15
16
17
18
19
20
21
22
23
24
25
26
27
28
29
30
31
32
33
34
35
36
37
38
39
40
41
42
43
44
45
46
47
48
49
50
51
52
53
54
55
56
57
58
59
60
61
62
63
64
65

515

[Figure 1 about here.]

1
2
3
4
5
6
7
8
9
10
11
12
13
14
15
16
17
18
19
20
21
22
23
24
25
26
27
28
29
30
31
32
33
34
35
36
37
38
39
40
41
42
43
44
45
46
47
48
49
50
51
52
53
54
55
56
57
58
59
60
61
62
63
64
65

516

[Figure 2 about here.]

1
2
3
4
5
6
7
8
9
10
11
12
13
14
15
16
17
18
19
20
21
22
23
24
25
26
27
28
29
30
31
32
33
34
35
36
37
38
39
40
41
42
43
44
45
46
47
48
49
50
51
52
53
54
55
56
57
58
59
60
61
62
63
64
65

517

[Figure 3 about here.]

1
2
3
4
5
6
7
8
9
10
11
12
13
14
15
16
17
18
19
20
21
22
23
24
25
26
27
28
29
30
31
32
33
34
35
36
37
38
39
40
41
42
43
44
45
46
47
48
49
50
51
52
53
54
55
56
57
58
59
60
61
62
63
64
65

518

[Figure 4 about here.]

1
2
3
4
5
6
7
8
9
10
11
12
13
14
15
16
17
18
19
20
21
22
23
24
25
26
27
28
29
30
31
32
33
34
35
36
37
38
39
40
41
42
43
44
45
46
47
48
49
50
51
52
53
54
55
56
57
58
59
60
61
62
63
64
65

519

[Figure 5 about here.]

1
2
3
4
5
6
7
8
9
10
11
12
13
14
15
16
17
18
19
20
21
22
23
24
25
26
27
28
29
30
31
32
33
34
35
36
37
38
39
40
41
42
43
44
45
46
47
48
49
50
51
52
53
54
55
56
57
58
59
60
61
62
63
64
65

520

[Figure 6 about here.]

1
2
3
4
5
6
7
8
9
10
11
12
13
14
15
16
17
18
19
20
21
22
23
24
25
26
27
28
29
30
31
32
33
34
35
36
37
38
39
40
41
42
43
44
45
46
47
48
49
50
51
52
53
54
55
56
57
58
59
60
61
62
63
64
65

521

[Figure 7 about here.]

1
2
3
4
5
6
7
8
9
10
11
12
13
14
15
16
17
18
19
20
21
22
23
24
25
26
27
28
29
30
31
32
33
34
35
36
37
38
39
40
41
42
43
44
45
46
47
48
49
50
51
52
53
54
55
56
57
58
59
60
61
62
63
64
65

522

[Figure 8 about here.]

1
2
3
4
5
6
7
8
9
10
11
12
13
14
15
16
17
18
19
20
21
22
23
24
25
26
27
28
29
30
31
32
33
34
35
36
37
38
39
40
41
42
43
44
45
46
47
48
49
50
51
52
53
54
55
56
57
58
59
60
61
62
63
64
65

523

[Figure 9 about here.]

1
2
3
4
5
6
7
8
9
10
11
12
13
14
15
16
17
18
19
20
21
22
23
24
25
26
27
28
29
30
31
32
33
34
35
36
37
38
39
40
41
42
43
44
45
46
47
48
49
50
51
52
53
54
55
56
57
58
59
60
61
62
63
64
65

524

[Figure 10 about here.]

1
2
3
4
5
6
7
8
9
10
11
12
13
14
15
16
17
18
19
20
21
22
23
24
25
26
27
28
29
30
31
32
33
34
35
36
37
38
39
40
41
42
43
44
45
46
47
48
49
50
51
52
53
54
55
56
57
58
59
60
61
62
63
64
65

525

[Figure 11 about here.]

List of Figures

- 1 The components of the experimental apparatus. (a) The schematic diagram of the bioreactor system including the locations of four scaffolds (left). The actual bioreactors and the connected tubes (right); (b) The Micro-CT scan of one scaffold specimen showing one large hole at its center; (c) 3D geometrical reconstruction of the scaffold surface from the high-resolution micro-CT scan. The inset shows the triangular surface mesh of the interconnected pores. 39
- 2 The experimental protocol for co-cultured hMSCs and prostate cancer (PCa) cells on the back surface of the scaffolds under static (right side) and dynamic (left side) conditions. The hMSCs were seeded on the scaffolds at Day-0 (control condition) before going through the culturing process for 23 days to promote extracellular matrix (ECM) formation. The PCa cells were then seeded on the bone ECM scaffolds on Day-23, and continued to grow under the respective static/dynamic conditions. 40
- 3 Computational configurations for four cases: A, B, C, and D (see Table 2). (a) Fluid flow in an empty bioreactor (Case A); and (b) The impact of four idealized scaffolds on the flow structure of the bioreactor (Case B). In Case C and D, the 3D geometrical model of the scaffolds from the micro-CT scan are used to compute fluid flow in pores; (c) Flow through the pores of one scaffold (Case C); (d) The impact of the second (downstream) scaffold on flow structures inside the first scaffold (Case D). The computational domains are defined as structured blocks as shown in Table 2. The red box indicates the area where the computational grid points are concentrated (around 40 millions points) to resolve individual pores. The computational domain includes two buffer regions near the inlet and outlet to ensure a realistic flow field surrounding the scaffolds. Flow is from the bottom to the top (black arrow). 41
- 4 The viability and proliferation of hMSCs assessed by WST-1 viability assay under static and dynamic culture: (a) Evaluated metabolic activity of hMSCs seeded on scaffold's front under dynamic culture by measuring the absorbance of color at 450 nm on Day-0 (Control), Day-5, and Day-10. $**p < 0.01$ indicates a significant difference between the Control and Day-10 dynamic samples; (b) Evaluated metabolic activity of hMSCs seeded on scaffold's back under dynamic culture and compared results with samples cultured under static conditions by measuring the absorbance of color at 450 nm on Day-0 (Control), Day-5, and Day-10. $*p < 0.05$ indicates a significant difference between Control and Day-5 samples and between Control and Day-10 samples. $\#p < 0.05$ indicates a significant difference between Day-5 static and Day-5 dynamic samples and between Day-5 static samples and Day-10 static samples. $§p < 0.05$ indicates a significant difference between Day-10 static and Day-10 dynamic samples. Error bars indicate standard deviation (SD). 42

1
2
3
4
5
6
7
8
9
10
11
12
13
14
15
16
17
18
19
20
21
22
23
24
25
26
27
28
29
30
31
32
33
34
35
36
37
38
39
40
41
42
43
44
45
46
47
48
49
50
51
52
53
54
55
56
57
58
59
60
61
62
63
64
65

566 5 The distribution, viability and orientation of the hMSCs were investigated
567 by nuclei DAPI staining (blue color), live-dead assay (green color), and SEM
568 analysis. (a) Schematic showing flow direction of media through bioreactor
569 accommodate with four scaffold samples. (b) DAPI Stained human mesenchy-
570 mal stem cells (hMSCs) nucleus representing distribution of cells on the back
571 side of the nanoclay-based scaffold grown under dynamic conditions on Day-23
572 (scale 1 mm). The cells are shown to posses high growth rate at the bound-
573 aries of the pores. (c) Live dead assay represents viability of hMSCs over 23
574 days under static and dynamic conditions, Scale 400 μm . (d) partial close-
575 up view of hMSCs grown on scaffold on Day-23. (e) SEM data represents
576 the random distribution of hMSCs under static culture on Day-23. (f) SEM
577 data represents the directional alignment of hMSCs under dynamic culture on
578 Day-23. 43

579 6 Images showing hematoxylin and eosin staining of hMSCs + MDAPCa2b
580 sequential culture on Day (23 + 20) represent variation in cells distribution
581 under (a, b) static culture and (c, d) dynamic culture at different scales. Yellow
582 arrows and red arrows indicate the location of tumor cells within the scaffold
583 and around the scaffold pores, respectively. 44

584 7 SEM data of hMSCs + MDAPCa2b sequential culture on Day (23 + 10)
585 (a and b) and Day (23+20) (c and d) represents morphological variations of
586 prostate cancer cells under (a, c) static culture and (b, d) dynamic culture.
587 Yellow arrows and red arrows indicate the location of tumor cells and scaffold
588 pores, respectively in the micrograph. (e) SEM data of hMSCs + MDAPCa2b
589 sequential culture on Day (23 + 20) indicating growth of tumor cells around
590 the scaffold pores under dynamic conditions. Yellow arrows indicate the loca-
591 tion of tumor cells around scaffold pores, in the micrograph. (f) the close-up
592 view of tumor cell growth around one pore. 45

593 8 Flow velocity distribution inside the bioreactor: (a) Case A (an empty biore-
594 actor); and (b) Case B (four idealized scaffolds). The velocity contours are
595 plotted on the plane of symmetry of the bioreactor. The flow velocity was ob-
596 served to remain low around 50 $\mu m/s$ inside the bioreactor chambers. With
597 the presence of idealized scaffolds, the flow velocity distribution is varied with
598 the magnitude up to 20 $\mu m/s$. The Flow-induced Shear Stress (FSS) direc-
599 tion on the surface of the four idealized scaffolds are shown in (c). Each
600 column represent the front and back of the idealized scaffold. The influence
601 of the gap between two consecutive scaffolds can be observed by creating a
602 FSS convergence zone on the surface with a magnitude between $[0 - 15] \mu Pa$. 46

603 9 The distribution of Fluid-induced Shear Stress (FSS) on the front (a), and
604 back (b) surfaces of one scaffold (Case C). The direction of the FSS indicated
605 a convergence pattern surrounding the pores on the front (c), and back (d)
606 surfaces. The insets illustrated the convergence of FSS vectors around the
607 pores. The histograms of flow velocity and FSS in the vicinity of the scaffold's
608 front and back surfaces were shown in (e) and (f), respectively. The vicinity
609 region was defined as a layer of 0.8 mm thickness from the corresponding
610 surface as shown in the inset of (e). 47

1
2
3
4
5
6
7
8
9
10
11
12
13
14
15
16
17
18
19
20
21
22
23
24
25
26
27
28
29
30
31
32
33
34
35
36
37
38
39
40
41
42
43
44
45
46
47
48
49
50
51
52
53
54
55
56
57
58
59
60
61
62
63
64
65

- 611 10 The hydrodynamic condition inside the scaffold at pore resolution (case C).
612 The interior flow (a) velocity magnitude and (b) Fluid-induced Shear Stresses
613 (FSS) within the scaffold were visualized from the transverse plane cuts at
614 25%, 50%, and 75% of the scaffold thickness (the horizontal inset). The flow
615 velocities and FSS were heterogeneously distributed in each cross-sectional
616 plane depending on the pore geometry. However, the frequency histograms
617 demonstrated that the (c) velocity and (d) FSS distribution exhibited a similar
618 pattern along the longitudinal (flow) direction. The majority of the flow
619 velocities were within the interval $[0.1 - 5] \mu m/s$, whereas the FSS was greater
620 than $1 \mu Pa$ 48
- 621 11 The hydrodynamic impacts of the second scaffold (case D): (a) Flow velocity
622 contour of the two full-scale scaffolds visualized from the plane of symmetry;
623 (b) The exact location of the 25%, 50% and 75% planes inside the first scaffold;
624 (c - d) Frequency histogram of the interior flow velocities and FSS of the first
625 scaffold taken from the horizontal plane cuts in (b). The flow velocities and
626 FSS within the first scaffold were observed to follow a similar trend as in the
627 single scaffold (case C) in Figure 10. 49

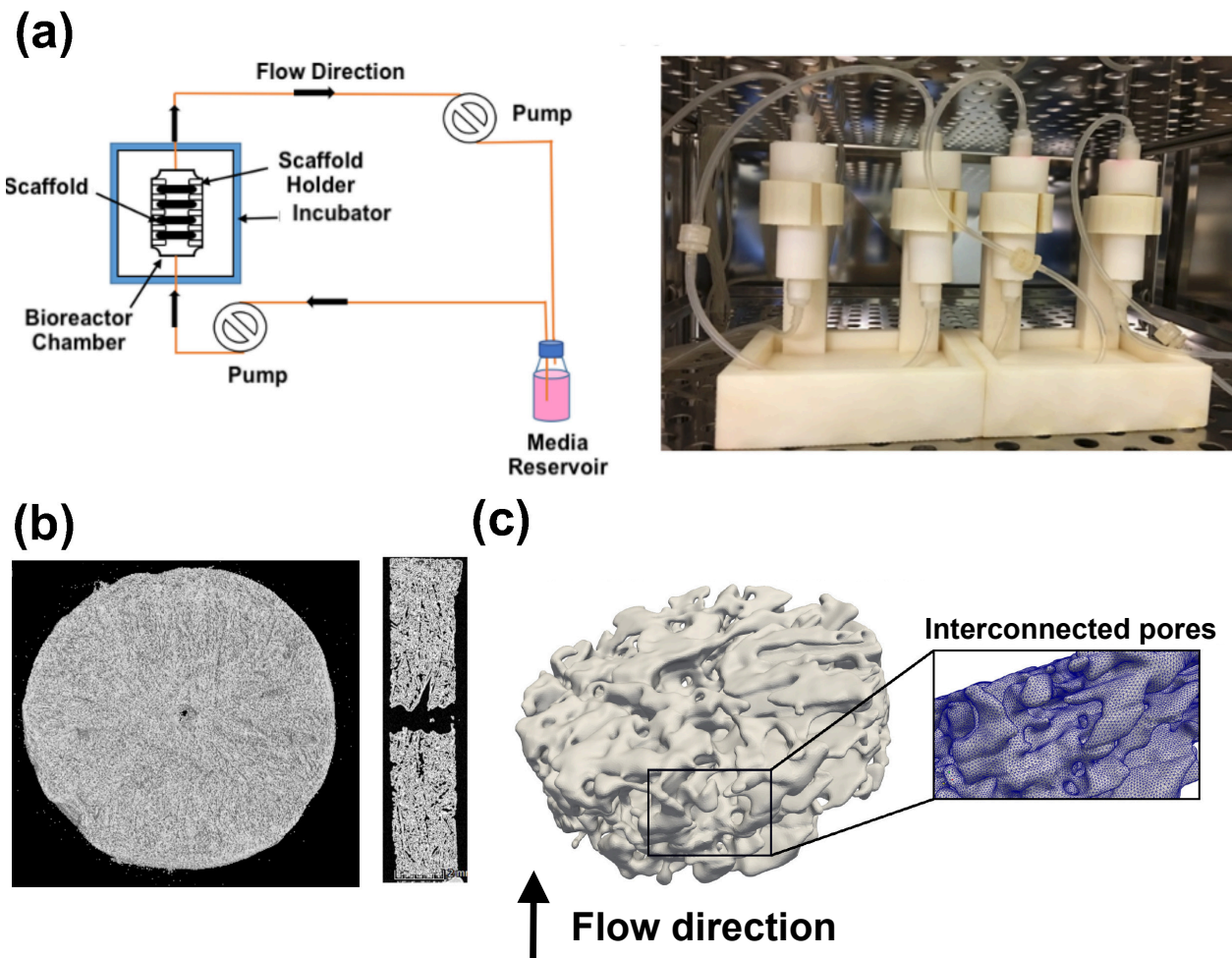


Figure 1: The components of the experimental apparatus. (a) The schematic diagram of the bioreactor system including the locations of four scaffolds (left). The actual bioreactors and the connected tubes (right); (b) The Micro-CT scan of one scaffold specimen showing one large hole at its center; (c) 3D geometrical reconstruction of the scaffold surface from the high-resolution micro-CT scan. The inset shows the triangular surface mesh of the interconnected pores.

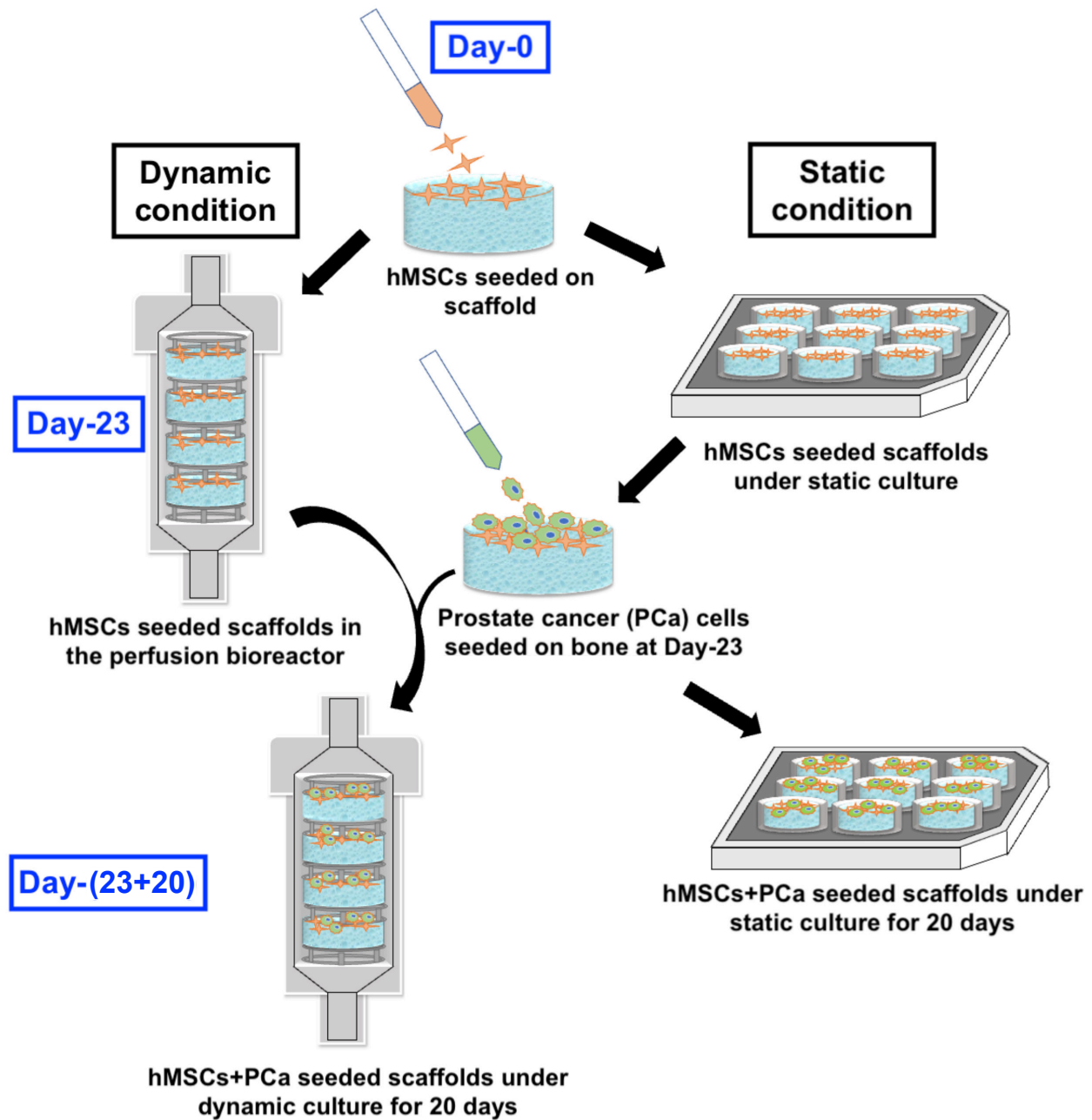


Figure 2: The experimental protocol for co-cultured hMSCs and prostate cancer (PCa) cells on the back surface of the scaffolds under static (right side) and dynamic (left side) conditions. The hMSCs were seeded on the scaffolds at Day-0 (control condition) before going through the culturing process for 23 days to promote extracellular matrix (ECM) formation. The PCa cells were then seeded on the bone ECM scaffolds on Day-23, and continued to grow under the respective static/dynamic conditions.

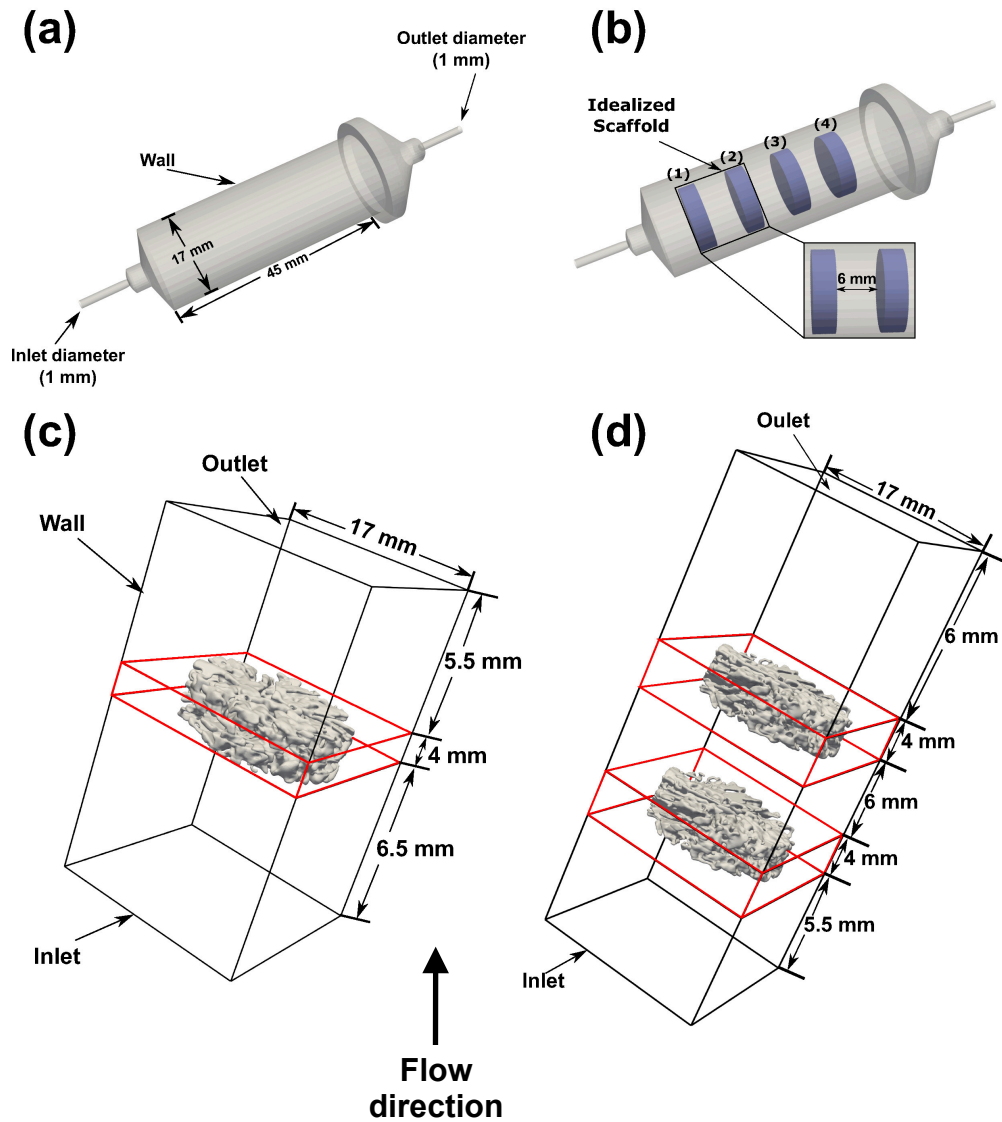


Figure 3: Computational configurations for four cases: A, B, C, and D (see Table 2). (a) Fluid flow in an empty bioreactor (Case A); and (b) The impact of four idealized scaffolds on the flow structure of the bioreactor (Case B). In Case C and D, the 3D geometrical model of the scaffolds from the micro-CT scan are used to compute fluid flow in pores; (c) Flow through the pores of one scaffold (Case C); (d) The impact of the second (downstream) scaffold on flow structures inside the first scaffold (Case D). The computational domains are defined as structured blocks as shown in Table 2. The red box indicates the area where the computational grid points are concentrated (around 40 millions points) to resolve individual pores. The computational domain includes two buffer regions near the inlet and outlet to ensure a realistic flow field surrounding the scaffolds. Flow is from the bottom to the top (black arrow).

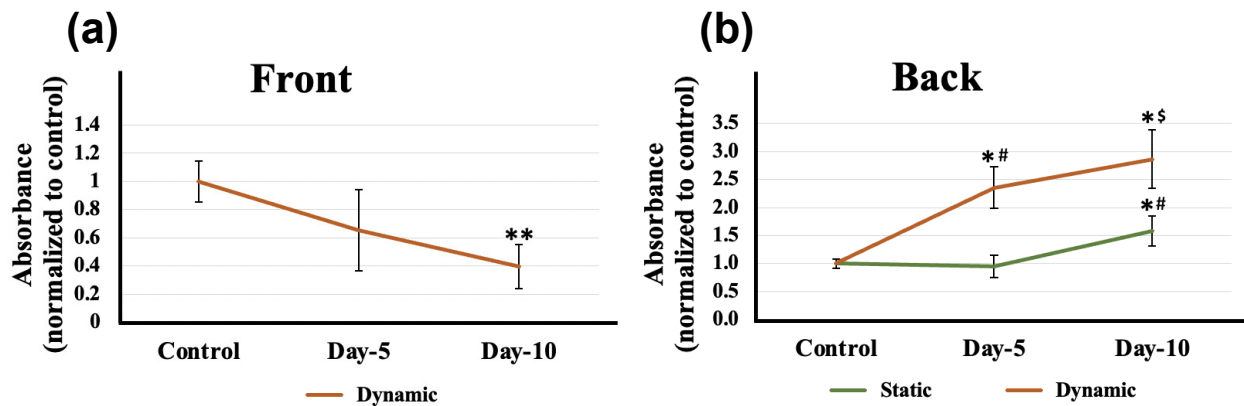


Figure 4: The viability and proliferation of hMSCs assessed by WST-1 viability assay under static and dynamic culture: (a) Evaluated metabolic activity of hMSCs seeded on scaffold's front under dynamic culture by measuring the absorbance of color at 450 nm on Day-0 (Control), Day-5, and Day-10. ** $p < 0.01$ indicates a significant difference between the Control and Day-10 dynamic samples; (b) Evaluated metabolic activity of hMSCs seeded on scaffold's back under dynamic culture and compared results with samples cultured under static conditions by measuring the absorbance of color at 450 nm on Day-0 (Control), Day-5, and Day-10. * $p < 0.05$ indicates a significant difference between Control and Day-5 samples and between Control and Day-10 samples. # $p < 0.05$ indicates a significant difference between Day-5 static and Day-5 dynamic samples and between Day-5 static samples and Day-10 static samples. § $p < 0.05$ indicates a significant difference between Day-10 static and Day-10 dynamic samples. Error bars indicate standard deviation (SD).

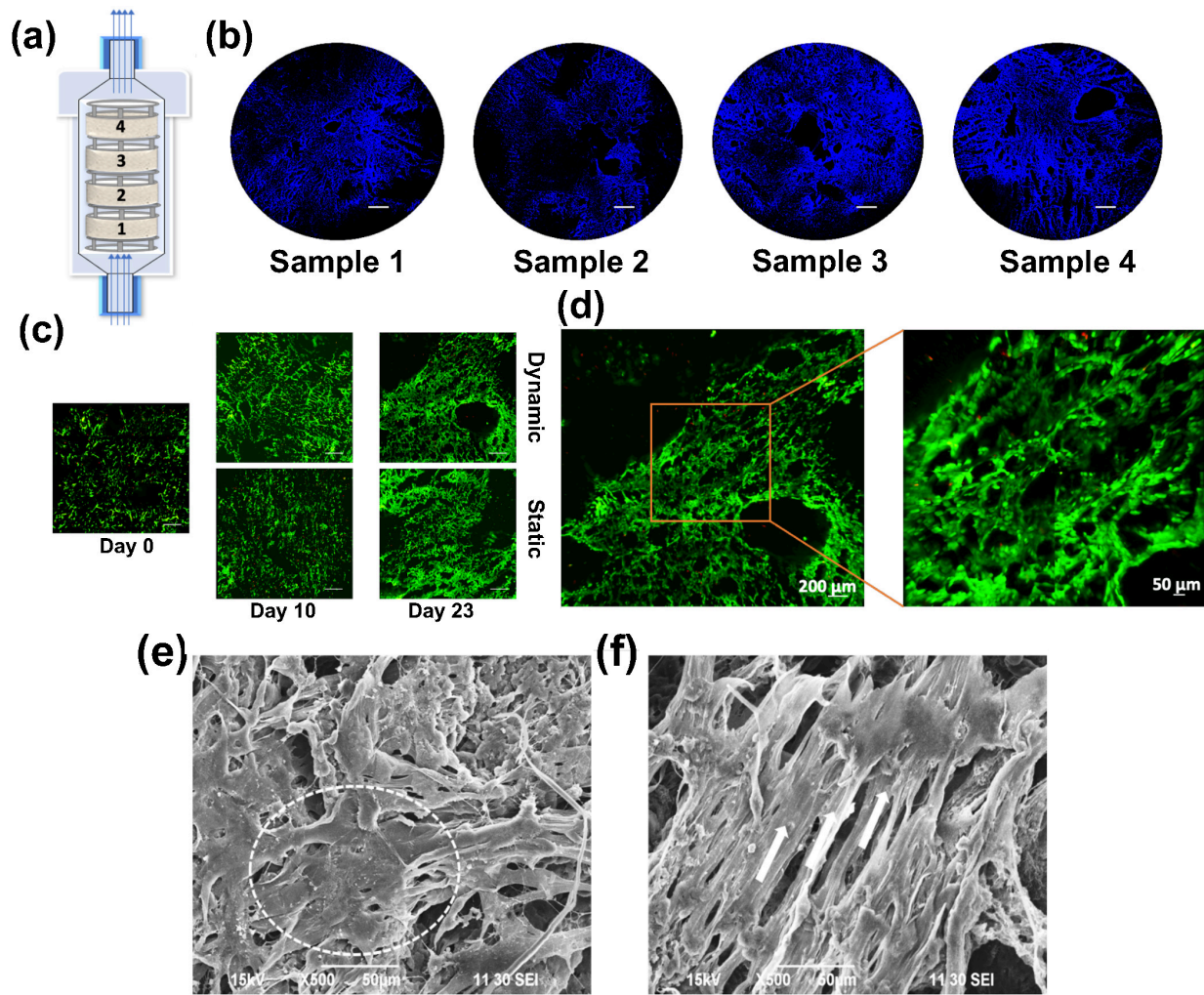


Figure 5: The distribution, viability and orientation of the hMSCs were investigated by nuclei DAPI staining (blue color), live-dead assay (green color), and SEM analysis. (a) Schematic showing flow direction of media through bioreactor accommodate with four scaffold samples. (b) DAPI Stained human mesenchymal stem cells (hMSCs) nucleus representing distribution of cells on the back side of the nanoclay-based scaffold grown under dynamic conditions on Day-23 (scale 1 mm). The cells are shown to possess high growth rate at the boundaries of the pores. (c) Live dead assay represents viability of hMSCs over 23 days under static and dynamic conditions, Scale 400 μm . (d) partial close-up view of hMSCs grown on scaffold on Day-23. (e) SEM data represents the random distribution of hMSCs under static culture on Day-23. (f) SEM data represents the directional alignment of hMSCs under dynamic culture on Day-23.

1
2
3
4
5
6
7
8
9
10
11
12
13
14
15
16
17
18
19
20
21
22
23
24
25
26
27
28
29
30
31
32
33
34
35
36
37
38
39
40
41
42
43
44
45
46
47
48
49
50
51
52
53
54
55
56
57
58
59
60
61
62
63
64
65

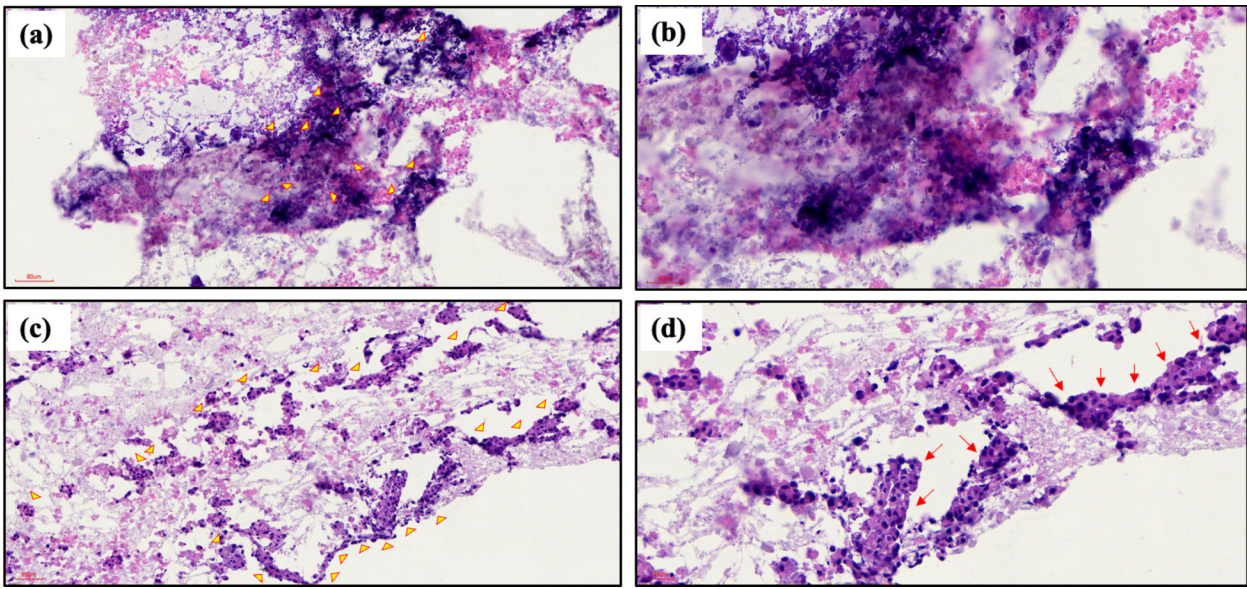


Figure 6: Images showing hematoxylin and eosin staining of hMSCs + MDAPCa2b sequential culture on Day (23 + 20) represent variation in cells distribution under (a, b) static culture and (c, d) dynamic culture at different scales. Yellow arrows and red arrows indicate the location of tumor cells within the scaffold and around the scaffold pores, respectively.

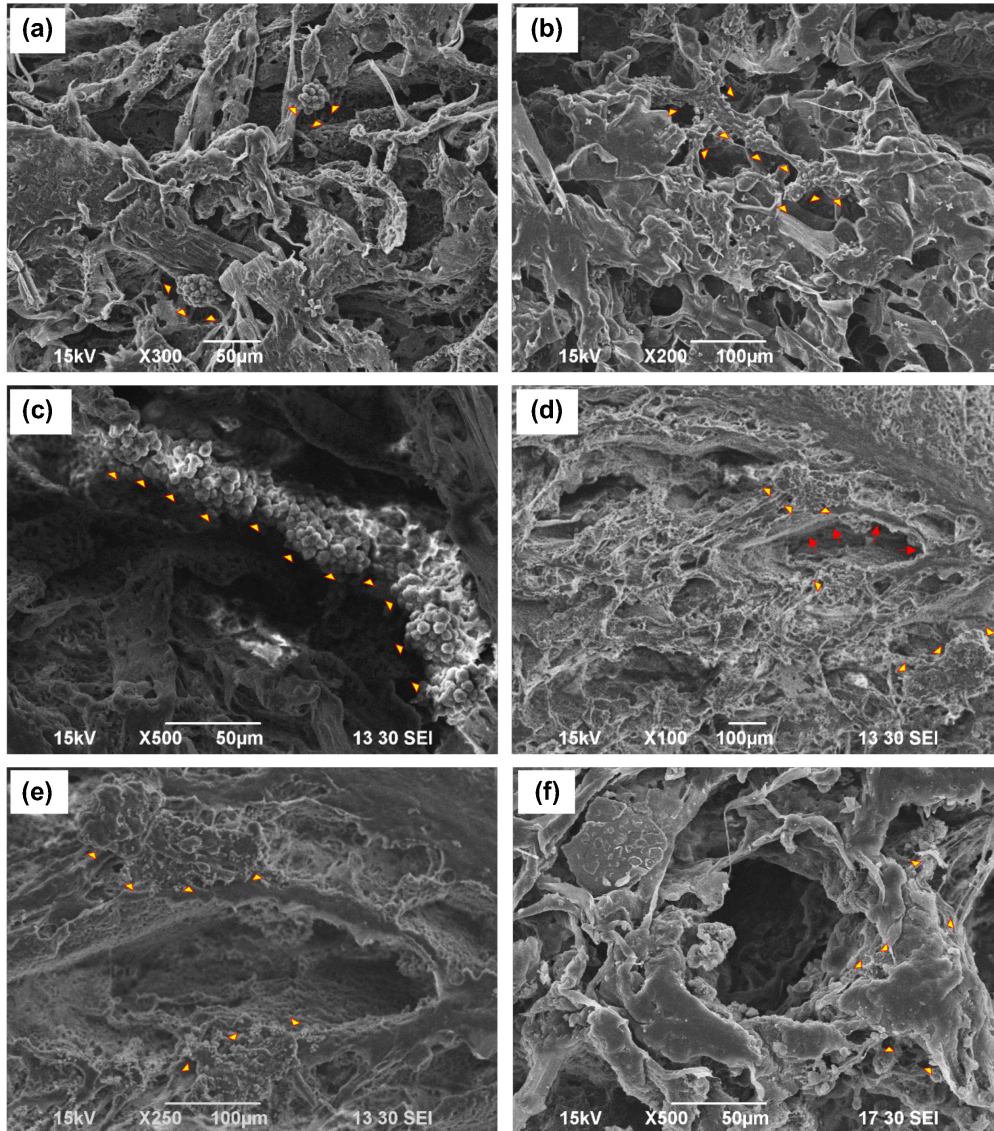


Figure 7: SEM data of hMSCs + MDAPCa2b sequential culture on Day (23 + 10) (*a* and *b*) and Day (23+20) (*c* and *d*) represents morphological variations of prostate cancer cells under (*a, c*) static culture and (*b, d*) dynamic culture. Yellow arrows and red arrows indicate the location of tumor cells and scaffold pores, respectively in the micrograph. (*e*) SEM data of hMSCs + MDAPCa2b sequential culture on Day (23 + 20) indicating growth of tumor cells around the scaffold pores under dynamic conditions. Yellow arrows indicate the location of tumor cells around scaffold pores, in the micrograph. (*f*) the close-up view of tumor cell growth around one pore.

1
2
3
4
5
6
7
8
9
10
11
12
13
14
15
16
17
18
19
20
21
22
23
24
25
26
27
28
29
30
31
32
33
34
35
36
37
38
39
40
41
42
43
44
45
46
47
48
49
50
51
52
53
54
55
56
57
58
59
60
61
62
63
64
65

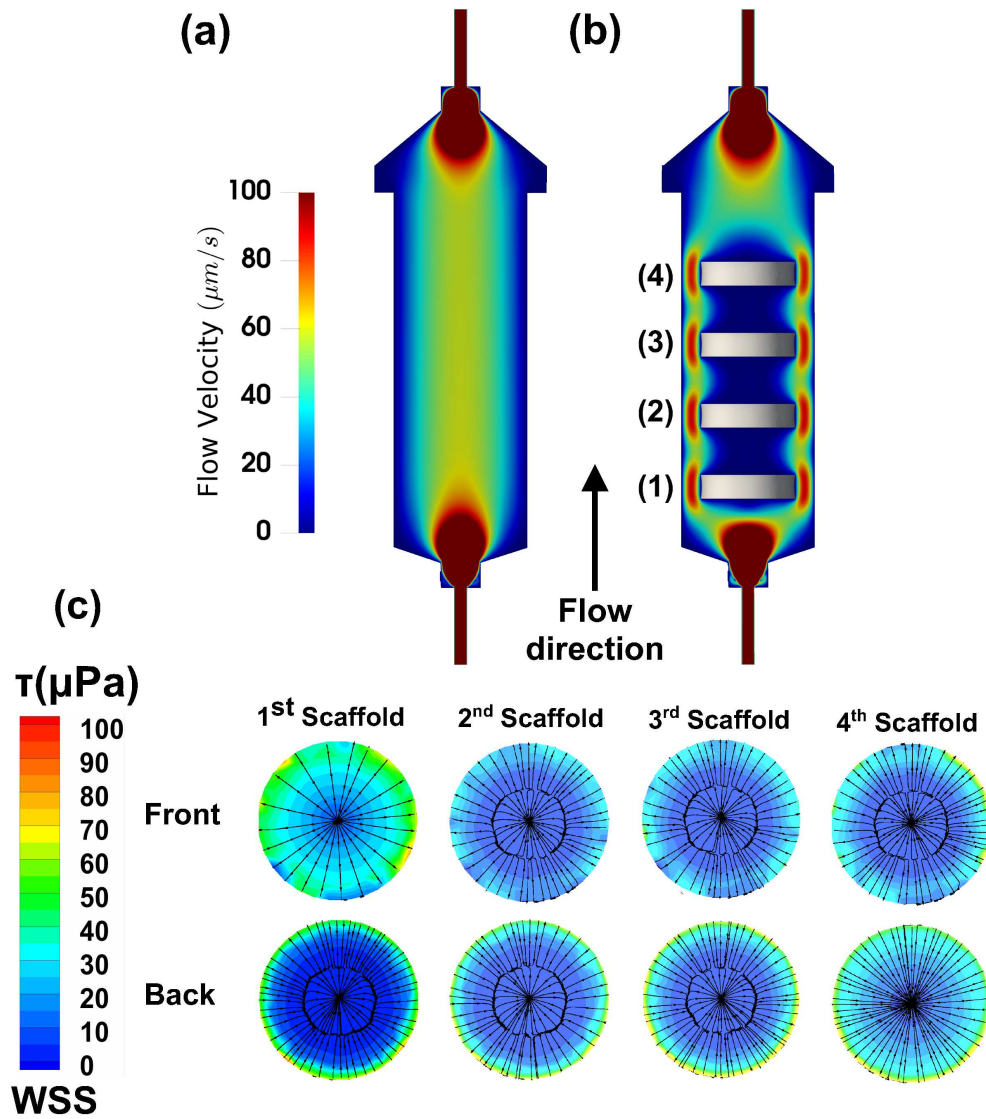


Figure 8: Flow velocity distribution inside the bioreactor: (a) Case A (an empty bioreactor); and (b) Case B (four idealized scaffolds). The velocity contours are plotted on the plane of symmetry of the bioreactor. The flow velocity was observed to remain low around $50 \mu\text{m/s}$ inside the bioreactor chambers. With the presence of idealized scaffolds, the flow velocity distribution is varied with the magnitude up to $20 \mu\text{m/s}$. The Flow-induced Shear Stress (FSS) direction on the surface of the four idealized scaffolds are shown in (c). Each column represent the front and back of the idealized scaffold. The influence of the gap between two consecutive scaffolds can be observed by creating a FSS convergence zone on the surface with a magnitude between $[0 - 15] \mu\text{Pa}$.

1
2
3
4
5
6
7
8
9
10
11
12
13
14
15
16
17
18
19
20
21
22
23
24
25
26
27
28
29
30
31
32
33
34
35
36
37
38
39
40
41
42
43
44
45
46
47
48
49
50
51
52
53
54
55
56
57
58
59
60
61
62
63
64
65

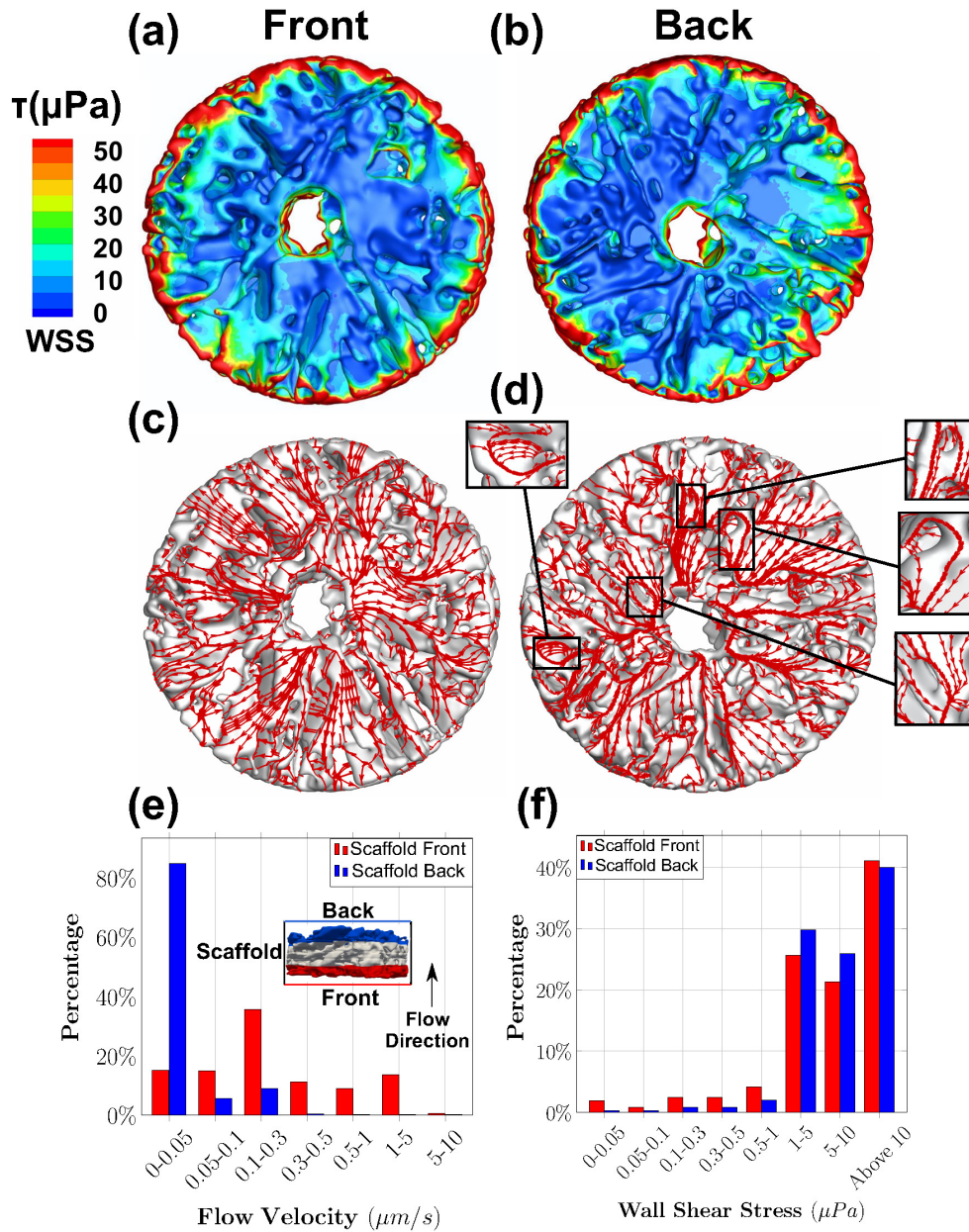


Figure 9: The distribution of Fluid-induced Shear Stress (FSS) on the front (a), and back (b) surfaces of one scaffold (Case C). The direction of the FSS indicated a convergence pattern surrounding the pores on the front (c), and back (d) surfaces. The insets illustrated the convergence of FSS vectors around the pores. The histograms of flow velocity and FSS in the vicinity of the scaffold's front and back surfaces were shown in (e) and (f), respectively. The vicinity region was defined as a layer of 0.8 mm thickness from the corresponding surface as shown in the inset of (e).

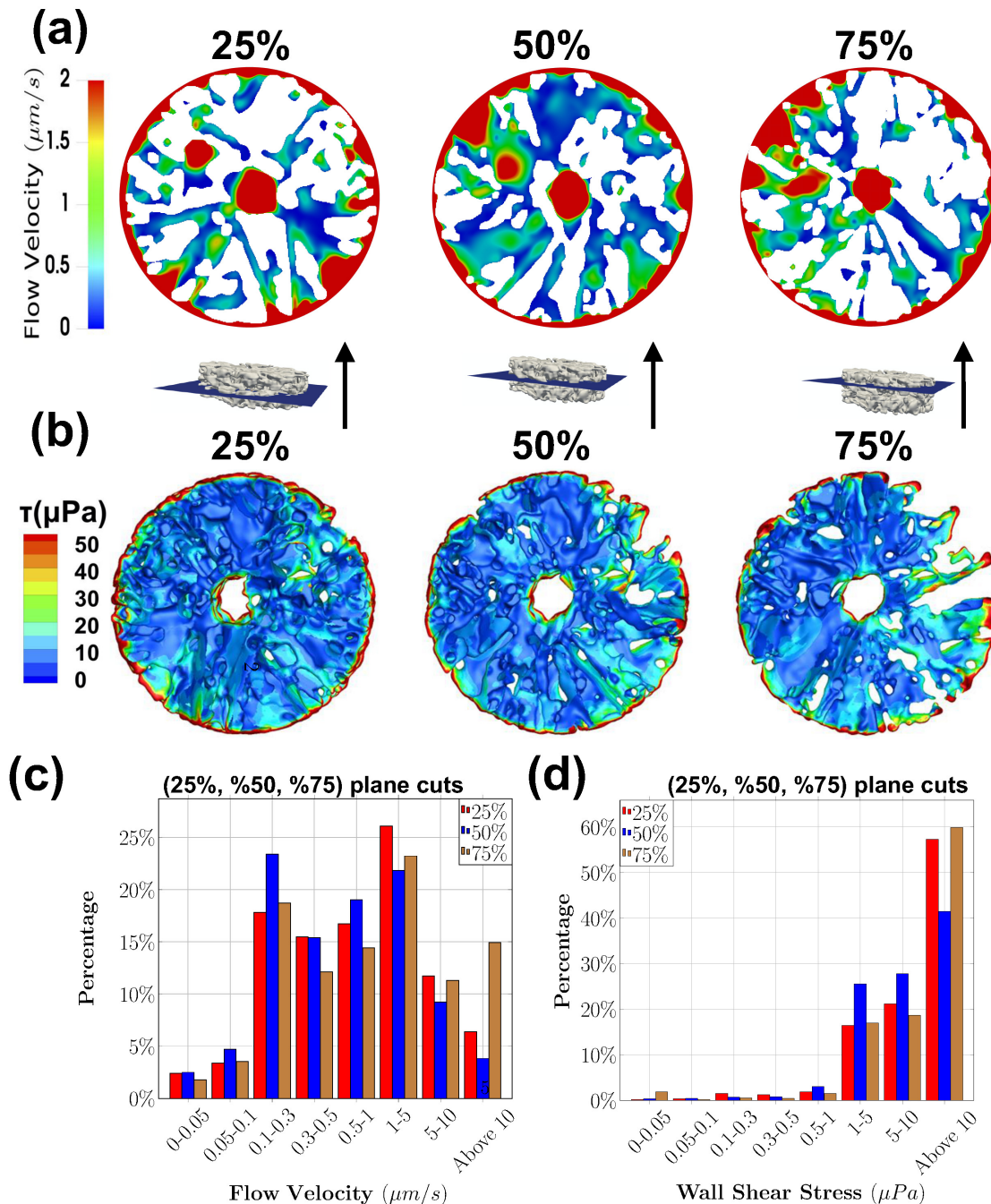


Figure 10: The hydrodynamic condition inside the scaffold at pore resolution (case C). The interior flow (a) velocity magnitude and (b) Fluid-induced Shear Stresses (FSS) within the scaffold were visualized from the transverse plane cuts at 25%, 50%, and 75% of the scaffold thickness (the horizontal inset). The flow velocities and FSS were heterogeneously distributed in each cross-sectional plane depending on the pore geometry. However, the frequency histograms demonstrated that the (c) velocity and (d) FSS distribution exhibited a similar pattern along the longitudinal (flow) direction. The majority of the flow velocities were within the interval $[0.1 - 5] \mu\text{m/s}$, whereas the FSS was greater than $1 \mu\text{Pa}$.

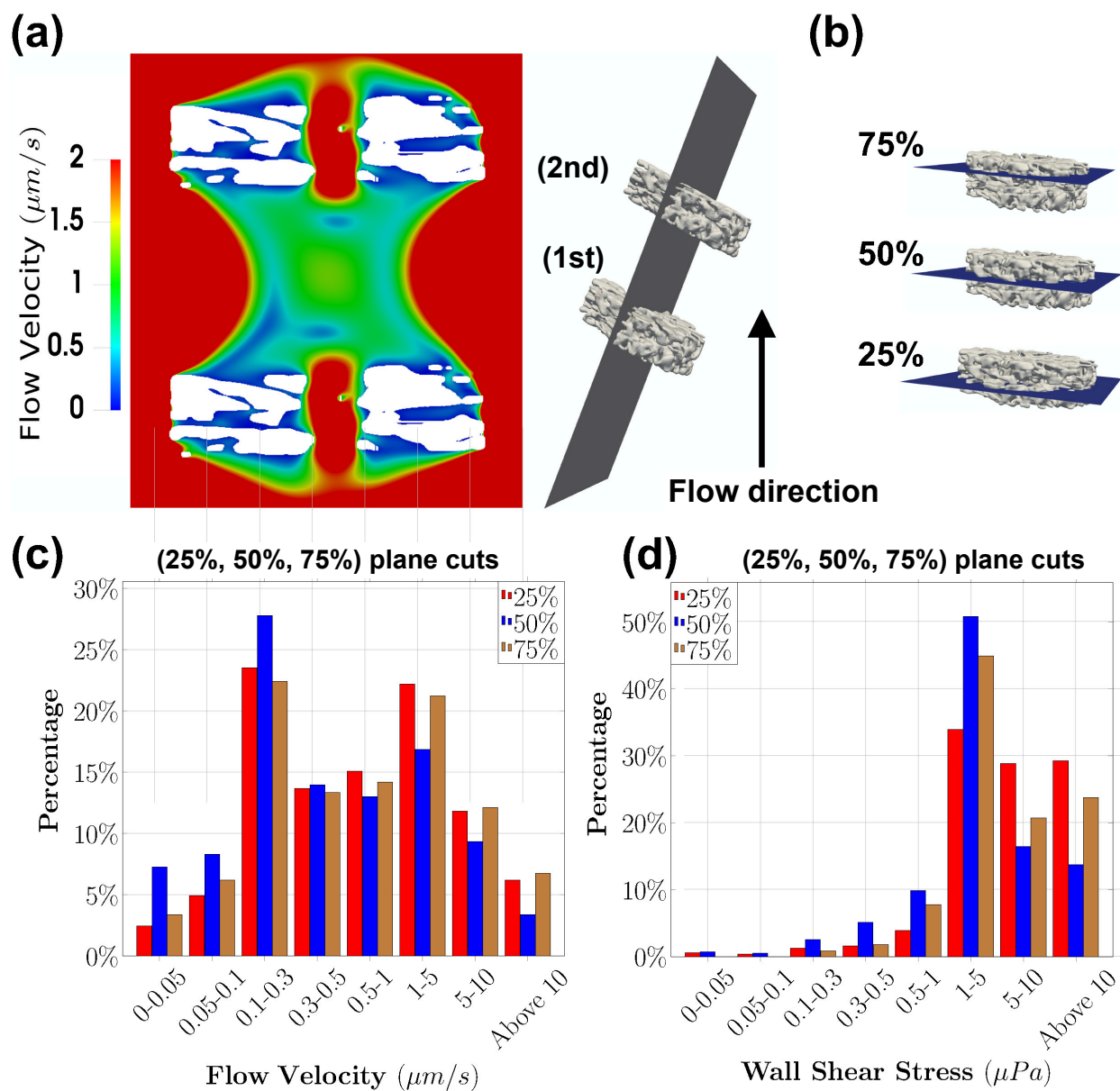


Figure 11: The hydrodynamic impacts of the second scaffold (case D): (a) Flow velocity contour of the two full-scale scaffolds visualized from the plane of symmetry; (b) The exact location of the 25%, 50% and 75% planes inside the first scaffold; (c–d) Frequency histogram of the interior flow velocities and FSS of the first scaffold taken from the horizontal plane cuts in (b). The flow velocities and FSS within the first scaffold were observed to follow a similar trend as in the single scaffold (case C) in Figure 10.

1
2
3
4
5
6
7
8
9
10
11
12
13
14
15
16
17
18
19
20
21
22
23
24
25
26
27
28
29
30
31
32
33
34
35
36
37
38
39
40
41
42
43
44
45
46
47
48
49
50
51
52
53
54
55
56
57
58
59
60
61
62
63
64
65

628 List of Tables

| | | | |
|-----|---|---|----|
| 629 | 1 | The details of surface meshes (triangular elements) for the bioreactor and the scaffolds (Figure 1) in numerical simulations (Figure 3). The surface meshes of the bioreactor and the idealized scaffold are generated from the geometric models using the commercial software Gridgen. The idealized scaffolds (Figure 3b) are considered as impervious cylinders. The geometry of the micro-CT scaffold is illustrated in Figure 1. | 51 |
| 630 | | | |
| 631 | | | |
| 632 | | | |
| 633 | | | |
| 634 | | | |
| 635 | 2 | Computational grids for numerical simulation of flows in the bioreactor: (a) Case A (the empty bioreactor); (b) Case B (the idealized scaffolds); (c) Case C (the micro-CT scaffold); (d) Case D (two full-scale scaffolds). The computational grid is a structured mesh of size $i \times j \times k$. The spatial grid resolution in the x, y , and z direction are $\Delta x, \Delta y$, and Δz , respectively. | 52 |
| 636 | | | |
| 637 | | | |
| 638 | | | |
| 639 | | | |

1
2
3
4
5
6
7
8
9
10
11
12
13
14
15
16
17
18
19
20
21
22
23
24
25
26
27
28
29
30
31
32
33
34
35
36
37
38
39
40
41
42
43
44
45
46
47
48
49
50
51
52
53
54
55
56
57
58
59
60
61
62
63
64
65

Table 1: The details of surface meshes (triangular elements) for the bioreactor and the scaffolds (Figure 1) in numerical simulations (Figure 3). The surface meshes of the bioreactor and the idealized scaffold are generated from the geometric models using the commercial software Gridgen. The idealized scaffolds (Figure 3b) are considered as impervious cylinders. The geometry of the micro-CT scaffold is illustrated in Figure 1.

| Surface mesh | Vertices | Elements |
|--------------------|----------|----------|
| Bioreactor | 3,759 | 7,518 |
| Idealized scaffold | 430 | 860 |
| Micro-CT scaffold | 276,913 | 555,086 |

1
2
3
4
5
6
7
8
9
10
11
12
13
14
15
16
17
18
19
20
21
22
23
24
25
26
27
28
29
30
31
32
33
34
35
36
37
38
39
40
41
42
43
44
45
46
47
48
49
50
51
52
53
54
55
56
57
58
59
60
61
62
63
64
65

Table 2: Computational grids for numerical simulation of flows in the bioreactor: (a) Case A (the empty bioreactor); (b) Case B (the idealized scaffolds); (c) Case C (the micro-CT scaffold); (d) Case D (two full-scale scaffolds). The computational grid is a structured mesh of size $i \times j \times k$. The spatial grid resolution in the x, y , and z direction are Δx , Δy , and Δz , respectively.

| Case | $i \times j \times k$ | $\Delta x \times \Delta y \times \Delta z$ (μm) | Total Grid Points |
|------|-----------------------------|--|-------------------|
| A | $351 \times 351 \times 351$ | $100 \times 80 \times 240$ | 43,243,551 |
| B | $351 \times 351 \times 351$ | $100 \times 80 \times 240$ | 43,243,551 |
| C | $401 \times 401 \times 491$ | $20 \times 20 \times 8$ | 64,481,201 |
| D | $401 \times 401 \times 537$ | $20 \times 20 \times 16$ | 86,350,137 |